molecules

MDPI

Article

Synergistic Al-MIL-53-(Mn) Bimetallic Metal–Organic Frameworks: Rational Tuning of Mn/Al Composition for Enhanced CO_2 Capture

Bulanga Djemima [1], Thulane Paepae [2], Oluwatayo Racheal Onisuru [1] and Major Melusi Mabuza [1,*]

[1] Department of Chemical Engineering, Faculty of Engineering and the Built Environment, University of Johannesburg, Johannesburg 2028, South Africa; djemimabl@gmail.com (B.D.); oluwatayo.onisuru@gmail.com (O.R.O.)

[2] Department of Mathematics and Applied Mathematics, Faculty of Science, University of Johannesburg, Johannesburg 2028, South Africa; tpaepae@uj.ac.za

* Correspondence: majorm@uj.ac.za; Tel: +27-11-559-6402

Abstract

The development of bimetallic metal–organic frameworks (BMOFs) represents a promising strategy to meet critical requirements of CO_2 capture in flue gas, where CO_2 exists at low partial pressure (0.15 bar, 298–333 K) due to the synergistic effects of mixed-metal incorporation that can enhance stability and CO_2 affinity. In this study, aluminum and manganese were coordinated on terephthalic acid to produce a series of bimetallic Al-MIL-53-(Mn) with varying Mn/Al molar ratios. These samples were synthesized via a hydrothermal approach, followed by a two-step activation, and characterized using FTIR, PXRD, SEM-EDX, TGA, and the BET method to uncover fundamental CO_2 adsorption characteristics. All samples exhibited MIL-53 features, including a predominant microporous structure, the presence of hydroxyl bridging groups in the surface chemistry, a rhomboidal morphology that supports their breathing behavior, and high thermal stability. The textural properties and the crystallinity were enhanced with increased mixed-metal ratios (Mn/Al = 0.15, 0.45, 0.65), and the findings revealed structural destabilization at a high molar ratio (Mn/Al = 0.85). Besides the 77 K low-pressure N_2 isotherms, CO_2 isotherms measured at a screening temperature of 273 K demonstrated a maximum uptake of 3.03 mmol/g, which compares favorably with the 2.19–2.85 mmol/g reported in the literature for pristine MIL-53(Al). They revealed a consistent Type I Langmuir isotherm with a steep uptake at low partial pressure, which suggests the presence of strong preferential binding sites for CO_2 on the surface of bimetallic MOFs. As this is a screening study, the bulk Mn content (ICP-OES), the CO_2/N_2 selectivity derived from 273 K and 298 K isotherms, the performance at flue-gas temperatures (313–333 K) and moisture tolerance remain to be established.

Keywords: metal–organic frameworks; CO_2 adsorption; post-combustion; bimetallic organic frameworks; hydrothermal synthesis

Academic Editors: Teng Zhang and Wenju Wang

Received: 25 September 2026
Revised: 2 November 2026
Accepted: 9 November 2026
Published: 12 November 2026

Copyright: © 2026 by the authors. Licensee MDPI, Basel, Switzerland. This article is an open access article distributed under the terms and conditions of the Creative Commons Attribution (CC BY) license.

1. Introduction

For CO_2 capture from combustion sources, notably coal-fired power plants, the industry relies on adsorption-based methods, primarily using amine solutions as the CO_2-absorbing medium [1]. This technology requires a high regeneration temperature, which

results in a high energy penalty, as well as solvent degradation and toxic effluent emissions challenges [2]. Consequently, research in physical adsorption, with the continuous development and improvement of solid sorbents aimed at high performance under conditions relevant to combustion environments, is increasingly emerging in Carbon Capture, Utilization, and Storage (CCUS) [3]. Metal–organic frameworks (MOFs), primarily produced by reactions between metal precursors and organic linkers to form metal–organic solid materials, are receiving substantial attention due to their exceptional physicochemical properties and versatile applications, such as gas storage [4].

Current studies focus on leveraging the structural tuneability of these materials to enhance adsorption capabilities under conditions relevant to flue-gas environments, where CO_2 exists at very low partial pressures (0.15 bar) [5]. Under these conditions, conventional adsorbents such as activated carbon, zeolites, and even pristine MOFs demonstrate inadequate performance due to the predominance of a physical adsorption mechanism that is primarily driven by van der Waals forces, which have been demonstrated to be relatively weak at low pressure [6,7]. Therefore, the concept of bimetallic MOF development in the MOF field extends the capacity of MOFs by introducing chemically distinct types of metal sites, rather than a greater number of them, whose different Lewis acidity and electron density modify the local environment of the CO_2 binding sites [8,9]. This is achieved through the synergistic effect between the two metals coordinated to a single linker, creating heterogeneous adsorption sites with different affinities to gas molecules [10]. One method is a co-assembly or direct synthesis method as described by Chen, Wang [11], which uses a single step to construct a secondary building unit (SBU) with two or more metal ions or two SBUs. Another method is post-synthetic modification (PSM), in which a second metal is introduced into a pre-formed pristine MOF after its synthesis, for example, by cation exchange or by grafting onto the framework [12].

During the last decade, pristine aluminum- and manganese-based MOFs have been successfully developed, exhibiting good performance in capturing CO_2. Al-MOFs have repeatedly exhibited excellent stability, attributed to the formation of an AlO_6 polyhedron that withstands high temperature [13]. For instance, Sun, Yin [14] prepared aluminum-based MIL-53 using a microwave-assisted solvothermal synthesis method. The framework temperature profile displayed a stable plateau going up to 480 °C. Han and Chakraborty [15] also reported that the Al-MOF developed was stable up to 418.5 °C, at which point the entire framework collapses. Moreover, Al-MOFs have demonstrated good hydrothermal stability, which enables their preparation in harsh synthesis and activation conditions. Correspondingly, Mn-MOF studies such as Sundriyal, Shrivastav [16] and Deng, Xu [17] which report the manganese-1,4-benzenedicarboxylate MOF (Mn-BDC) and Asghar, Iqbal [18] which reports the Mn–DABDC (2,5-diaminoterephthalate) describe excellent redox flexibility that partly stems from their multiple oxidation states (Mn^{2+}, Mn^{3+}, Mn^{4+}), which provide more electronic coordination chemistry for CO_2.

Based on their individual mechanistic and experimentally demonstrated potential, this study explored this synergistic combination for the development of a bimetallic MOF, aiming to enhance CO_2 adsorption properties. The successful synthesis of a bimetallic MOF depends on the metal compatibility, which has a significant effect on the resulting crystallinity and textural properties. The compatibility of different metal elements within a single MOF structure has been investigated systematically, particularly for frameworks built from rod-shaped SBUs such as MIL-53. Depending on the relative size, charge, and coordination preferences of the cations, the metals may be distributed homogeneously, arranged in specific sequences within the SBUs, or segregated into separate domains or crystals [8,11,19–21]. Moreover, the use of pre-formed heterometallic molecular complexes as building units has enabled the incorporation of a divalent metal (Ni^{2+}) into the trivalent-metal rod SBU of the MIL-53-type framework MIL-69 [22]. However, studies

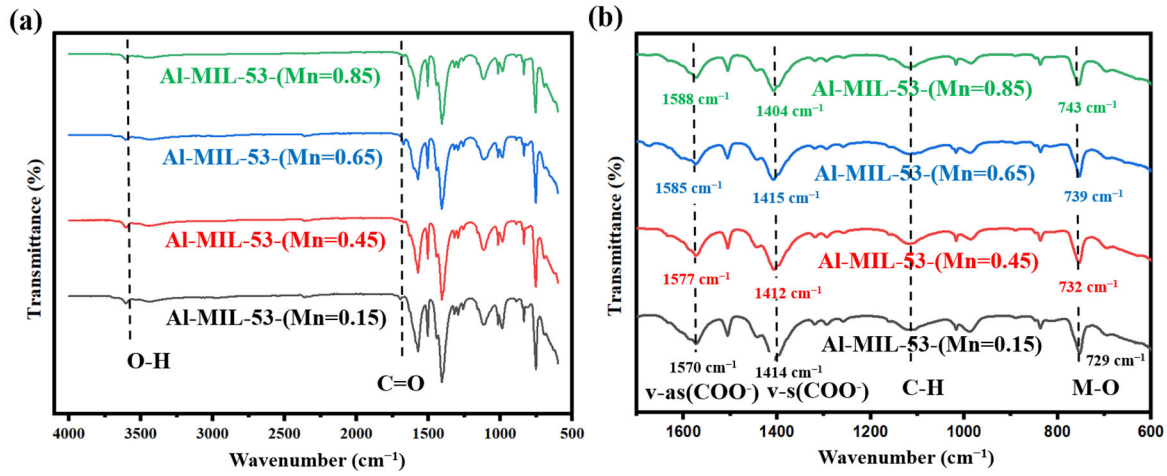
addressing the combination of Al^{3+} and Mn^{2+} remain scarce. This study verified and supported the use of aluminum and manganese based on the presence of a previously reported study by Wang, Jiang [23], which incorporated Al/Mn, although the resulting framework was applied for trace benzene removal rather than CO_2 removal, alongside the work of Abid, Rada [12]. In addition, the mixed-metal ratio is also a major parameter that influences physicochemical properties. Therefore, this study employed varying mixed-metal ratios to investigate the effect, with the addition of the utilization of water as the mother liquor for synthesis.

2. Results

2.1. Surface Chemistry

The distinct surface characteristics of the synthesized Al-MIL-53 MOFs revealed by FTIR analysis are depicted in Figure 1, suggesting successful carboxylate and metal–oxygen coordination, as well as the efficiency of the activation process. More specifically, during the hydrothermal synthesis of Al-MIL-53-(Mn), a high quantity of unreacted TPA was observed after synthesis due to low solubility of TPA in water as reported by Abid and colleagues [12]. TPA displays strong intermolecular hydrogen binding and $\pi - \pi$ interactions that strengthen its crystal structure, and it possesses hydrophobic aromatic rings that reduce its polarity [24]. Moreover, water molecules can be coordinated with metal centers via interaction with vacant Lewis acid sites or bridging hydroxyl groups [25]. These molecules are located on the framework's external surface and block access to the pores for CO_2 [26]. Hence, the activation method enabled the removal of unreacted TPA and coordinated solvent molecules as shown in Figure 1a, with evidence of weak O-H stretching and C=O peaks, respectively, in the 3000–3500 cm^{-1} and 1650–1730 cm^{-1} regions across all the samples, which is similar to the report of [27].

The visible O-H peaks are associated with characteristic μ_2-OH bridging groups of the MIL-53 structure, through which O-bonded complexes are formed with CO_2 during adsorption [28]. Figure 1b, an expanded version of Figure 1a in the 1600–600 cm^{-1} region, clearly reveals that carboxylic functional groups appear within the band region of 1650–1400 cm^{-1}. The firm asymmetric stretching COO^- peaks at 1570 cm^{-1} for Al-MIL-53-(Mn = 0.15), 1577 cm^{-1} for the Al-MIL-53-(Mn = 0.45), 1585 cm^{-1} for Al-MIL-53-(Mn = 0.65), and 1588 cm^{-1} for Al-MIL-53-(Mn = 0.85) and the symmetric stretching vibrations of COO^- are observed at 1414 cm^{-1} for Al-MIL-53-(Mn = 0.15), 1412 cm^{-1} for Al-MIL-53-(Mn = 0.45), 1415 cm^{-1} for Al-MIL-53-(Mn = 0.65), and 1404 cm^{-1} for Al-MIL-53-(Mn = 0.85). Collectively, these reflections are ascribed to the deprotonation of the -COOH groups of the terephthalate linker, confirming successful ligand coordination with Al^{3+} and Mn^{2+} metal nodes [29].



https://doi.org/10.3390/molecules31224087

Figure 1. FTIR spectra of Al-MIL-53-(Mn = 0.15, 0.45, 0.65, 0.85): (**a**) full spectra range (4000–500 cm^{-1}); (**b**) characteristics bands (1600–600 cm^{-1}).

Although the primary adsorption sites of CO_2 are attributed to the hydroxyl groups of MIL-53, the COO^- vibrations critically modulate the electronic environment of the adsorbent for augmented adsorption [30]. M-O (metal–oxygen) signals appear in the characteristic region of 750–500 cm^{-1}, indicating metal incorporation into the framework with peaks at 729 cm^{-1} for the Al-MIL-53-(Mn = 0.15), 732 cm^{-1} for the Al-MIL-53-(Mn = 0.45), 739 cm^{-1} for Al-MIL-53-(Mn = 0.65), and 743 cm^{-1} for Al-MIL-53-(Mn = 0.85). Furthermore, the spectra revealed a gradual decrease in peak intensity as the Mn^{2+} content increased, notably for the symmetric stretching of COO^- groups and bridging hydroxyl units. This is attributed to Mn^{2+} acting as a Lewis acid, which coordinates with carboxylate and carbonyl groups, thereby altering their electron density. This phenomenon is reported to weaken the bond force constants of the C=O and O-H group oscillators, resulting in a reduction in their vibrational frequencies [31]. The effects of Mn^{2+} incorporation are also observed in the metal–oxygen region, whereby Mn^{2+} coordination to the carboxylate oxygens and Al-oxo chains results in the creation of Al-O-C and Mn-O-C locales. Mn^{2+} possesses partially filled d-orbitals that allow stronger electronic alterations of the local bonding environment, resulting in the introduction of structural defects that influence both the crystallinity and adsorption properties of Mn-modified MIL-53. This is consistent with the report by Wang, Jiang [23] on the surface chemistry of hetero-valent Al^{3+}/Mn^{2+}. However, the absence of a pronounced wavenumber shift indicated that only a small fraction of M-O oscillators involved Mn, which is in agreement with the low degree of framework incorporation inferred from the unchanged PXRD patterns in Section 2.2. Thus, despite the reduced vibrational intensities, the framework remains dominated by Al-O vibrations of the $AlO_4(OH)_2$ chains.

2.2. Crystalline Profile

The XRD patterns of Al-MIL-53-(Mn = 0.15, 0.45, 0.65, 0.85) are presented in Figure 2a, which shows a single phase corresponding to the MIL-53 large-pore (lp) crystal structure, verifying the integrity and phase purity of Al-MIL-53-(Mn) [12]. The crystalline profile of Al-MIL-53, as documented in the COD (4108535) and CCDC (220477) reference files [32], exhibits characteristic diffraction peaks at approximately $2\theta \approx 9.34°$, 12.58°, 17.76°, 25.20°, and 27.16°, corresponding to the (110), (200), (020), (202), and (220) crystal planes, respectively [29]. The overall characteristic peaks of Al-MIL-53-(Mn) align closely with these reference reflections, confirming the successful formation of well-crystallized Al-MIL-53-(Mn) frameworks under the applied synthesis conditions. Notably, the PXRD patterns of all four samples are nearly identical despite the wide range of nominal Mn^{2+}/Al^{3+} ratios (0.15–0.85) used in the synthesis mixture, and no reflections attributable to crystalline manganese oxides or separate Mn-terephthalate phases were detected. This indicates that the amount of Mn retained in the activated frameworks is considerably lower than the nominal synthesis ratio, which is in agreement with a closely related bimetallic MIL-53 system in which only 0.37–1.53 wt% Mn was retained after activation despite high mixed-metal ratios in the synthesis mixture [12].

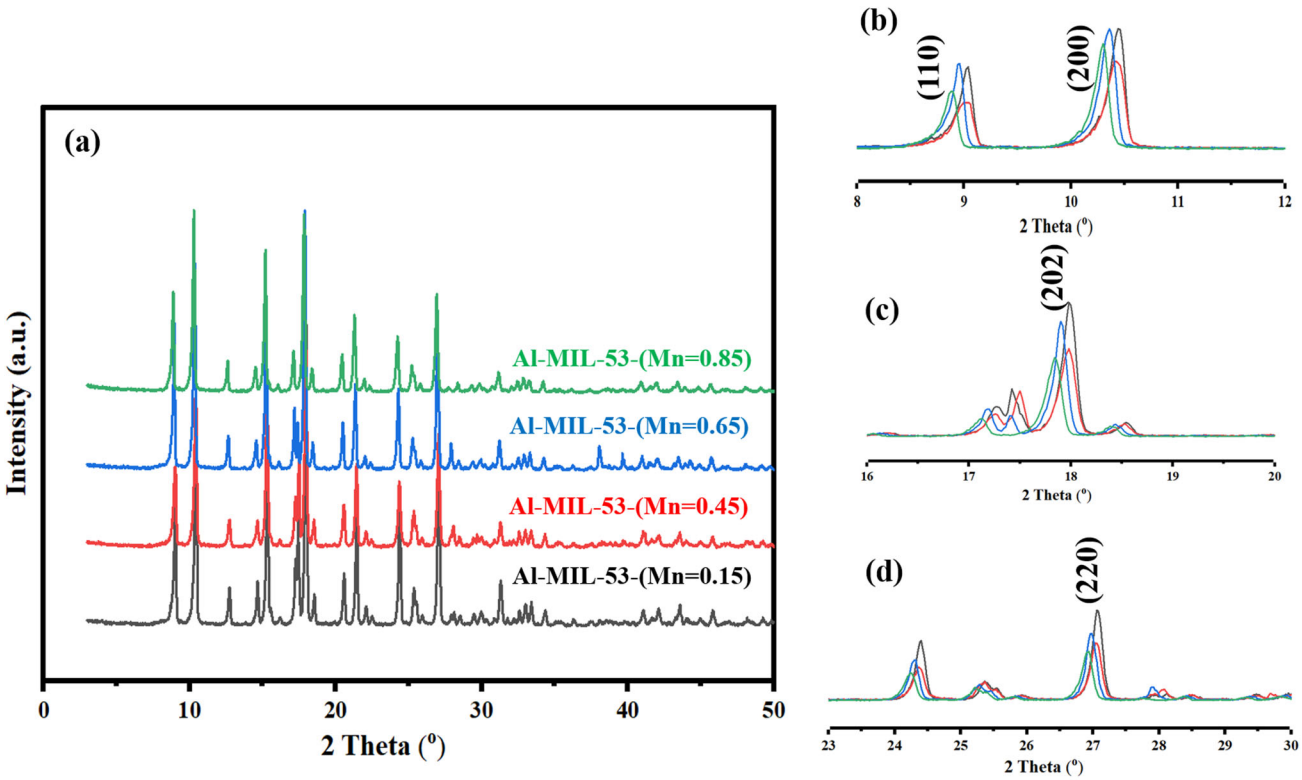


Figure 2. PXRD of Al-MIL-53-(Mn = 0.15, 0.45, 0.65, 0.85): (**a**) 0–50°, (**b**) 8–12° panel displaying (110) and (200) crystal planes, (**c**) 16–20° panel displaying (202) crystal plane, (**d**) 23–30° displaying (220) crystal plane.

The effect of varying Mn^{2+}/Al^{3+} content was further emphasized through the slight shifts in 2θ values reflecting local lattice strain as displayed in Figure 2b–d. These patterns confirm the effect of the heterogeneous ion distribution induced by Mn^{2+} incorporation and resemble the previously reported structure of the modified MIL-53 by Abid, Rada [27]. For instance, the Al-MIL-53-(Mn = 0.65) sample displayed peaks at 2θ = 8.88°, 10.3°, 17.85°, 24.26°, and 26.94°, while Al-MIL-53-(Mn = 0.45) showed characteristic peaks at 2θ = 9.07°, 10.46°, 17.52°, 24.41°, and 27.09°. The corresponding (110) d-spacings calculated from Bragg's law varied only between 9.74 and 9.95 Å across the series as displayed in Table 1, confirming that the MIL-53 framework was preserved and that the shifts reflect framework flexibility rather than a change in crystal structure. The degree crystallinity assessed from FWHM of the (110), which narrowed from 0.18° to 0.14° along the Scherrer crystalline size, increased from 44.3 to 56.9 nm, indicating improved long-range order. However, the highest Mn^{2+}-loaded sample (Al-MIL-53-(Mn = 0.85)) showed the broadest (110) reflection (FWHM = 0.23°) and the smallest crystalline domain size (34.6 nm), indicating a loss of long-range order and partial destabilization of the MOF structure. Similarly, Deng, Liu [33] reported that increasing Mn loading in a bimetallic Mg-Mn-MOF progressively reduced the peak intensity and led to complete structural degradation. This behavior is attributed to the formation of structural defects associated with Mn^{2+} species located at the Al-oxo chains and carboxylate sites. While such defects may introduce additional unsaturated metal sites, the evident reduction in crystallinity reflects that lattice distortion dominates at high Mn^{2+} synthesis loading. This structural disruption limits the MIL-53 structure integrity and ultimately governs the reduced textural properties revealed by the N_2 and CO_2 adsorption tests on the Al-MIL-53-(Mn = 0.85) [27,34,35].

Table 1. Calculated crystallite size of the Al-MIL-53-(Mn) samples using the Scherrer equation and Bragg's law for the MIL-53 characteristic (110) crystal plane.

MOF Samples	2θ (°)	d calc (Å)	FWMH (°)	Bragg Angle θ	β (rad)	D Scherrer (nm)
Al-MIL-53-(Mn = 0.15)	8.99	9.82	0.18	4.5	0.0031	44.30
Al-MIL-53-(Mn = 0.45)	9.07	9.74	0.16	4.53	0.0027	49.80
Al-MIL-53-(Mn = 0.65)	8.88	9.94	0.14	4.44	0.0024	56.90
Al-MIL-53-(Mn = 0.85)	9.03	9.79	0.23	4.48	0.0039	34.60

2.3. Morphology and Elemental Composition

The morphologies of the Al-MIL-53-(Mn) samples depicted in Figure 3 showed faceted rhomboidal crystals, with a uniform size in the 2–5 μm range, typical of porous MIL-53 structures [12]. A noticeable change in crystal size and a gradual loss of uniformity was observed with the increase in Mn^{2+} content. This behavior is consistent with the growth-modulating character of heteroatom systems, which include alterations in the nucleation and crystal growth kinetics [36,37]. As evidenced by the PXRD results, the introduction of bimetallic nodes induces lattice distortions and defects within the framework, thereby limiting crystal growth and favoring the formation of smaller crystals.

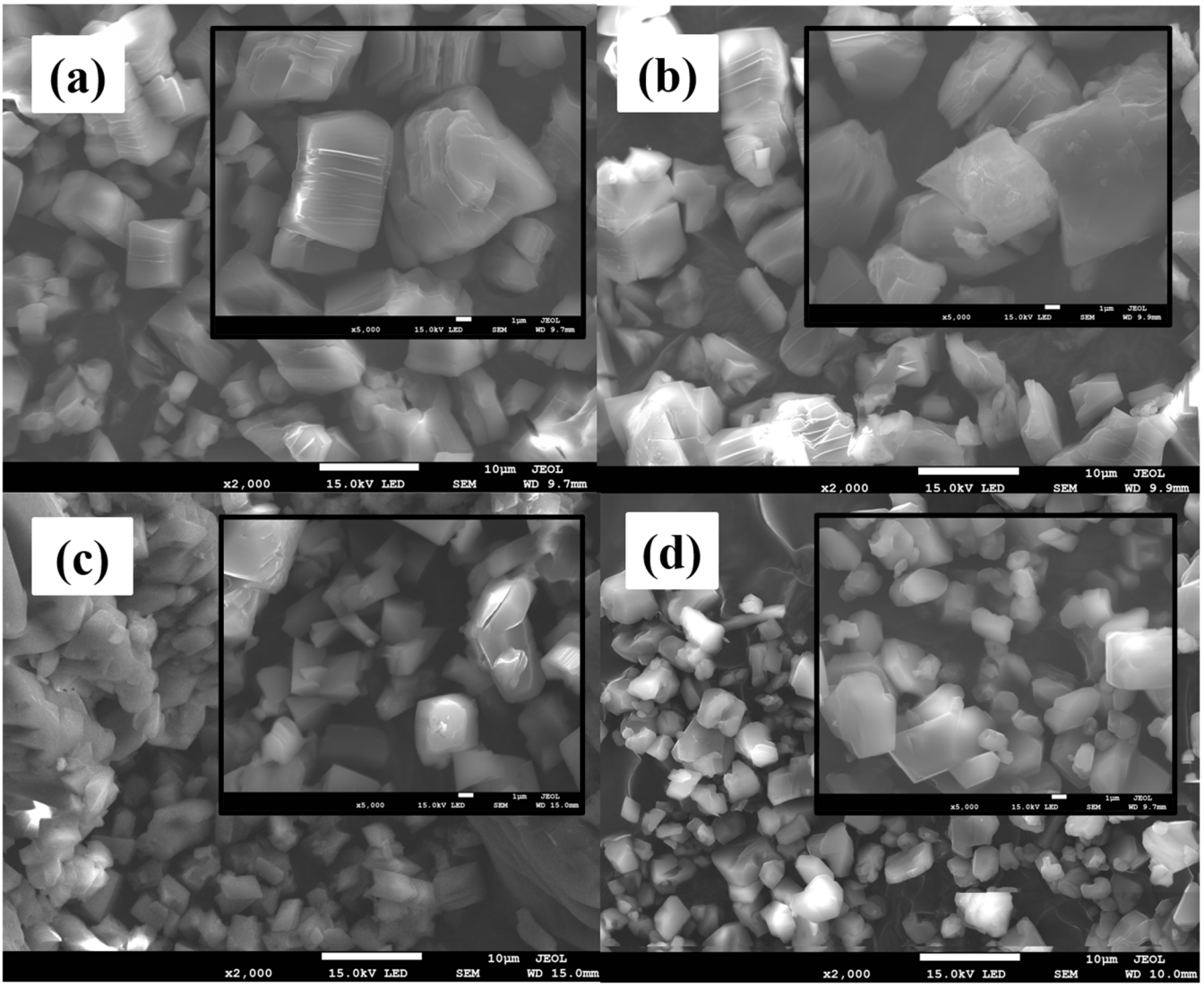


Figure 3. SEM micrographs: (**a**) Al-MIL-53-(Mn = 0.15), (**b**) Al-MIL-53-(Mn = 0.45), (**c**) Al-MIL-53-(Mn = 0.65), (**d**) Al-MIL-53-(Mn = 0.85).

The EDX analysis across different spots, as depicted in Figure 4a–d, reflected the local distribution of the metals in the samples and confirmed the presence of both Al and Mn in all samples. While the C and O atomic compositions remained relatively uniform, Al^{3+} and Mn^{2+} varied noticeably, which suggested the surface heterogeneity of all Al-MIL-53-(Mn) samples. This heterogeneity is attributed to the differences in the coordination chemistry of Al^{3+} and Mn^{2+} during the synthesis. Al^{3+} and Mn^{2+} are different in coulombic force, atomic size, and coordination geometry. Al^{3+} exhibits a smaller ionic radius, allowing faster hydrolysis and nucleation compared to Mn^{2+}, which displays slower coordination kinetics. Moreover, this mismatch in charge, ionic radius and coordination also limits the substitution of Mn^{2+} into the Al-oxo chains, and weakly bound Mn^{2+} is likely removed during the DMF and ethanol solvent exchange, which together account for a low Mn retention inferred from the PXRD patterns. The observed surface heterogeneity suggested that the pore channel of the bimetallic MOF is not chemically uniform, and this is owing to different Lewis acidities and electron densities, thereby offering multiple adsorption sites with different affinities for CO_2 molecules [38]. Surface heterogeneity is a desirable outcome in the development of bimetallic MOFs, as it is associated with enhanced binding strength, but it also emphasized the need for reticular chemistry investigation of these materials to identify their topological features.

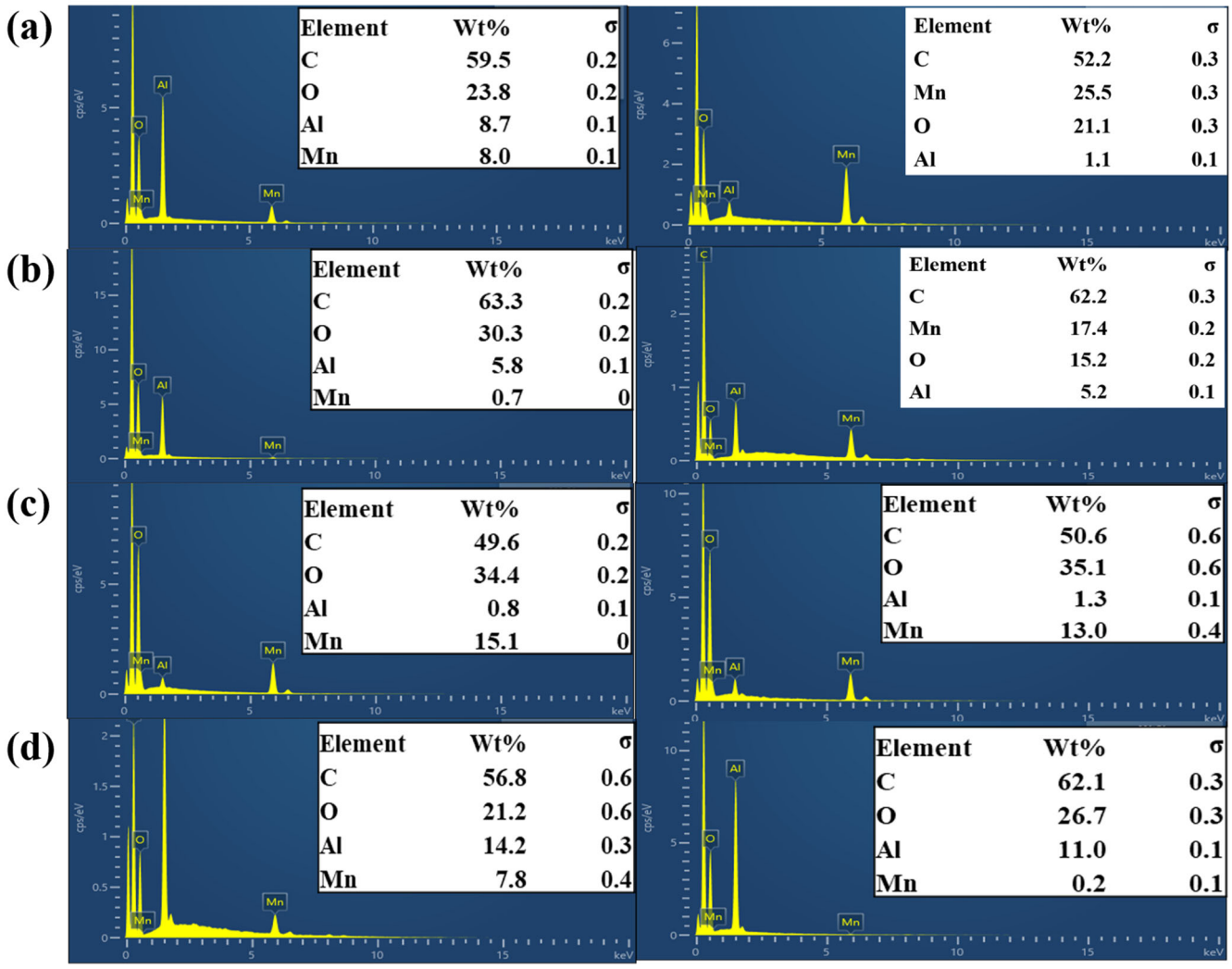


Figure 4. EDX spectra recorded at two distinct sites of (**a**) Al-MIL-53-(Mn = 0.15), (**b**) Al-MIL-53-(Mn = 0.45), (**c**) Al-MIL-53-(Mn = 0.65), (**d**) Al-MIL-53-(Mn = 0.85).

2.4. Temperature Profile

The thermogravimetric analysis of the bimetallic Al-MIL-53-(Mn) samples is shown in Figure 5, depicting the temperature profile of the synthesized MOFs after activation at 150 °C. The material exhibited a similar three-stage decomposition process across all samples (Mn = 0.15 to 0.85), suggesting that the low level of Mn^{2+} retained in the framework did not alter the Al-O carboxylate bond environment of traditional Al-MIL-53 SBUs, as supported by FTIR, PXRD, and low-pressure N_2/CO_2 adsorption tests. An initial mass loss was observed at low temperature, corresponding to the removal of guest molecules, mainly water that had been physically adsorbed and DMF confined within the samples' frameworks, which underwent desorption upon heating [39]. The relatively small loss (~3–5%) suggests low solvent retention after activation, which is consistent with the FTIR results. This is, in addition, consistent with the hydrophilic nature of the μ_2-OH bridging groups in MIL-53, which facilitate hydrogen bonding with guest molecules [30]. The next step, ranging from ~150 to 550 °C, exhibited a pronounced thermal plateau, suggesting the absence of decomposition events in this temperature region. This behavior is considered diagnostic of framework stability and is attributed to the strong Al^{3+} carboxylate coordination bonds, aligning with Pearson's hard–soft acid-base (HSAB) theory, whereby the hard Lewis acidity of Al^{3+} yields robust metal–oxygen bonds that resist thermal dissociation [40].

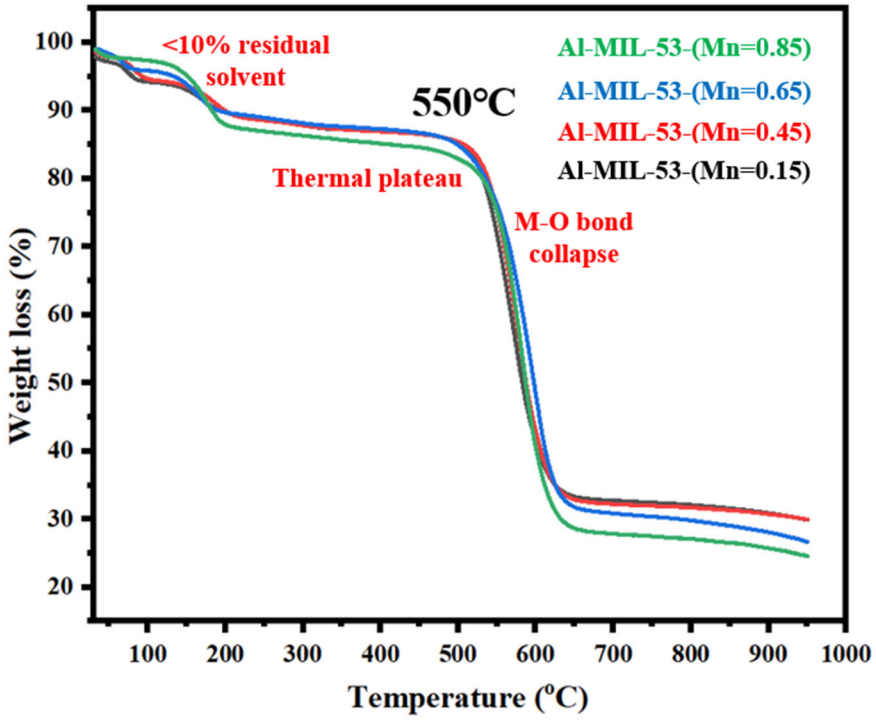


Figure 5. Thermogravimetric analysis (TGA) of Al-MIL-53-(Mn = 0.15), Al-MIL-53-(Mn = 0.45), Al-MIL-53-(Mn = 0.65) and Al-MIL-53-(Mn = 0.85).

The thermal analysis revealed that all samples withstood heating to ~550 °C. Such a high decomposition temperature is considered quite unusual for the large family of MOFs and suggests the bimetallic Al-MIL-53-(Mn) is a robust framework [41]. The material displayed better thermal stability than HKUST-1, which collapses at 240 °C [42], UiO-66, which collapses at 250 °C [42], MIL-100, which collapses in the range of 250–400 °C, and MOF-74 analogs, which collapse in the 200–400 °C region [43]. No distinct intermediate weight loss associated with the release of trapped impurities, including unreacted TPA and residual metal oxides, was observed in the plateau region. The absence of these

features was indicative of phase purity, as reflected by the PXRD analysis, and emphasized the necessity of the two-step activation procedure [12]. The main weight loss was observed in the temperature range of ~550–650 °C. This sharp, sigmoidal mass loss is associated with the thermal decomposition of the organic linker and the irreversible collapse of the framework due to the breaking of the metal–ligand bond [43].

2.5. Textural Properties

2.5.1. Low-Pressure N_2 Adsorption on Al-MIL-53-(Mn)

The textural properties of Al-MIL-53-(Mn) samples were evaluated at 77 K, and the corresponding surface areas, pore volumes, micropore volumes, and micropore content are summarized in Table 2**.** The nitrogen adsorption and desorption isotherms of all Al-MIL-53-(Mn) samples displayed in Figure 6 exhibited Type IV behavior, characterized by a steep uptake at low pressures ($p/p_0 < 0.1$, where p is the equilibrium pressure and p_0 is the saturation vapor pressure of the adsorbate at the analysis temperature, ≈101.3 kPa for N_2 at 77 K) due to the primary microporous nature of the material (pore size < 2 nm). The Type IV assignment refers specifically to the intermediate-pressure branch and hysteresis loop, which arise from secondary textural mesoporosity and framework breathing, while the low-pressure region retains the Type I characteristic. This is consistent with the characteristic pore structure of MIL-53 systems, justifying the study's sample designation [34].

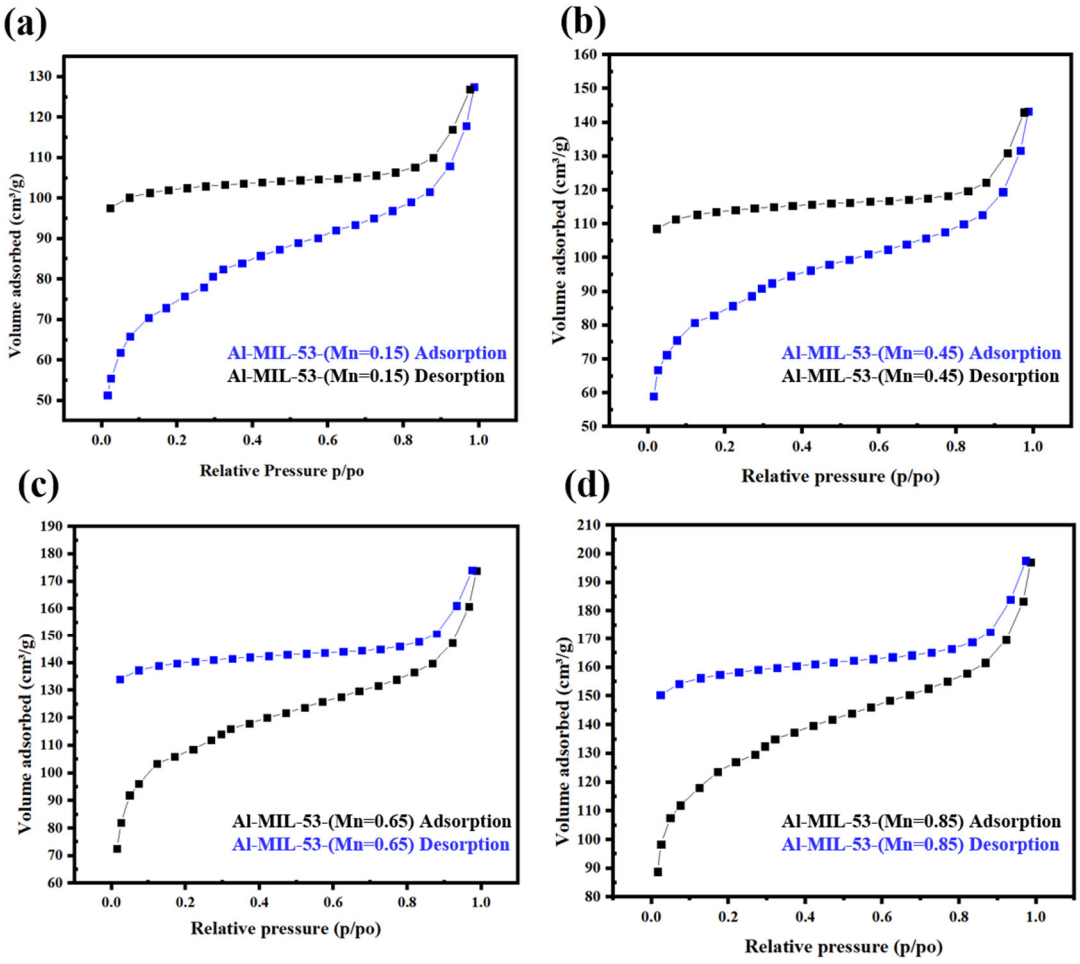


Figure 6. Low-pressure N_2 adsorption and desorption isotherms on (**a**) Al-MIL-53-(Mn = 0.15), (**b**) Al-MIL-53-(Mn = 0.45), (**c**) Al-MIL-53-(Mn = 0.65), (**d**) Al-MIL-53-(Mn = 0.85).

Further, the N_2 adsorption–desorption isotherms all exhibited pronounced open hysteresis loops with H4 character consistent across all samples and a gradual increase in adsorption at intermediate pressure. This phenomenon reflects the well-established breathing effect associated with the MIL-53 topology, involving the adsorbent's reversible transition between large-pore (lp) and narrow-pore (np) states upon the adsorption of guest molecules [44]. During uptake of the N_2 gas, the framework pores expand, and on desorption, the framework contracts at a different pressure threshold. Additionally, the isotherms integrate the H4 type according to the IUPAC classification, confirming that Al-MIL-53-(Mn) is a flexible microporous material. This flexibility arises from the μ_2-OH bridging groups connecting the Al^{3+} octahedral chains.

At moderate Mn^{2+} loading (Mn^{2+}/Al^{3+} = 0.45 and 0.65), the open hysteresis loop remained relatively narrow, confirming the electronic effect of Mn^{2+} around the metal nodes and carboxylate linkers; however, the highest Mn content sample exhibited a widening of the loop, confirming the increased lattice distortion and defect formation, reflected by the XRD results [36].

Table 2. Textural properties derived from low-pressure N_2 adsorption on Al-MIL-53-(Mn).

	SA_{BET} (m^2/g)	SA_{DFT} (m^2/g)	Pore Volume (cm^3/g)	Micropore Volume (cm^3/g)	Micropore Content (%)
Al-MIL-53-(Mn = 0.15)	246.0	419.8	0.127	0.074	58.2
Al-MIL-53-(Mn = 0.45)	276.9	472.9	0.143	0.089	62.1
Al-MIL-53-(Mn = 0.65)	347.8	581.6	0.174	0.118	67.9
Al-MIL-53-(Mn = 0.85)	451.4	784.9	0.296	0.157	53.4

The surface area was enhanced with increased Mn^{2+} content, ranging from 246.0 to 451.4 m^2/g with the DFT method displaying 419.8 m^2/g, 472.9 m^2/g, 581.6 m^2/g, and 784.9 m^2/g, respectively for Al-MIL-53-(Mn = 0.15, 0.45, 0.65, 0.85) as depicted in Table 2**.** These values indicate that the non-reacted and exchangeable Mn^{2+} might play a supplementary role as a template similar to the role of the solvent, thereby promoting defect formation and development of additional porosity [37]. The obtained surface area values exceeded those reported for bimetallic systems such as the Zn/Ce-MOF (15.6 m^2/g), Zn/Cu-BTC (15.6 m^2/g), and Mg/Zn-MOF-74 (55 m^2/g and 24.73 m^2/g) [45,46]. Samples with higher Mn^{2+} showed increasing pore volume, correspondingly from 0.127 to 0.296 cm^3/g, which is indicative of defect creation and framework expansion rather than a partial blocking of pores by Mn^{2+} ions. Comparable effects of heteroatom incorporation have been reported in Mn-MOFs [33]. Figure 7 displays the pore size distribution (PSD) of all Al-MIL-53-(Mn) samples, obtained with the DFT method for the micropore region (Figure 7a) and the BJH method for the mesopore region (Figure 7b). The average pore diameter was determined to be 1.6 nm across all samples, corresponding to the micropores in the samples.

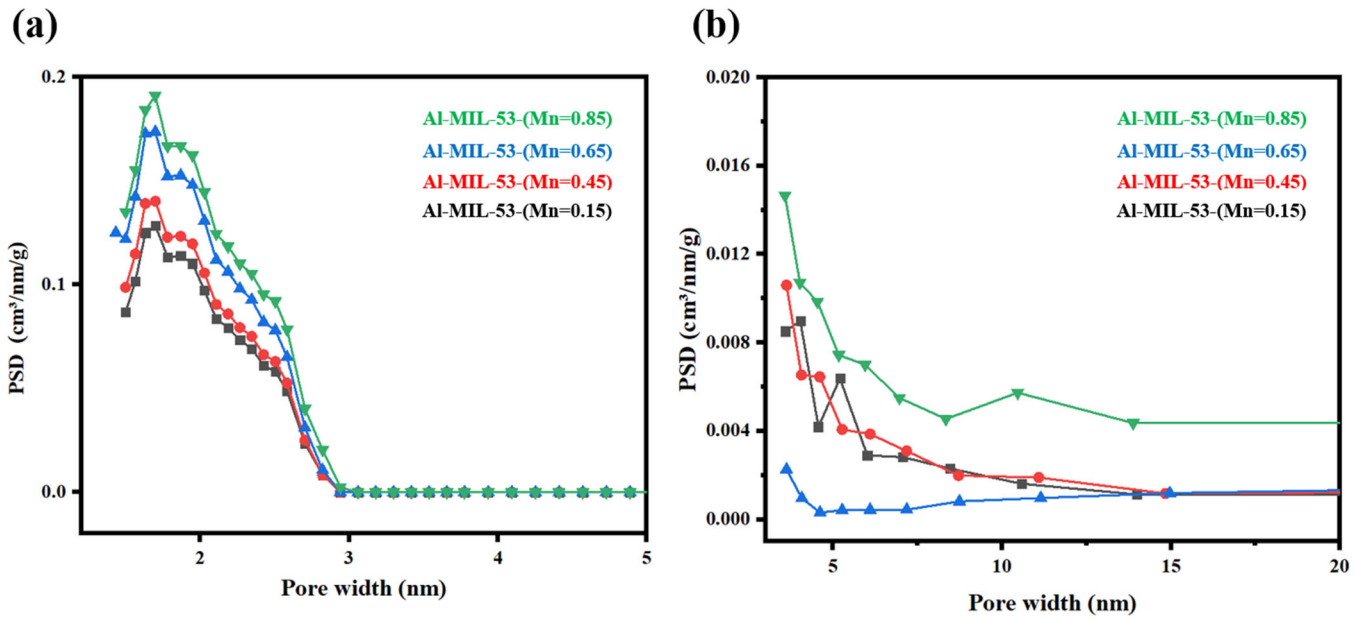


Figure 7. Pore size distribution of Al-MIL-53-(Mn = 0.15, 0.45, 0.65, 0.85) samples; (**a**) micropores (DFT method) and (**b**) mesopores (BJH method).

The finding was consistent with the study by Abid, Rada [12], which reported an average pore diameter of 1.5 nm for all samples and aligned with the adsorption isotherms confirming the predominant microporous nature of the samples. The mesopore size distribution revealed distinct characteristics associated with Mn^{2+} incorporation; the mesopore radius of Al-MIL-53-(Mn = 0.15) and Al-MIL-53-(Mn = 0.45) ranged from 3.58 to 4.03 nm, while Al-MIL-53-(Mn = 0.65) displayed the lowest radius of 3.21 nm. In contrast, Al-MIL-53-(Mn = 0.85) exhibited the highest mesopore distribution, ranging from 3.2 nm to 5.95 nm, consistent with the reduction in micropore content (53.4%) reported in Table 2**.** This emphasized the formation of defects and the increased surface heterogeneity observed in PXRD, FTIR, and SEM analyses. This structural modification aligns with previous reports on bimetallic MOF systems [34].

2.5.2. Low-Pressure CO_2 Adsorption on Al-MIL-53-(Mn) Samples

The low-pressure CO_2 adsorption isotherms of Al-MIL-53-(Mn) samples are depicted in Figure 8**,** indicating that there is no significant variation in the behavior of Al-MIL-53-(Mn) with different Mn^{2+} loadings. All samples showed steep uptake at low pressure ($p/p_0 < 0.01$), indicating strong interaction between the heterogeneous MOF surface and CO_2 gas. Correspondingly, the CO_2 isotherms also exhibited a closed-loop Type I isotherm, consistent with the microporous adsorption reflected by the low-pressure N_2 adsorption. Further, a noticeable hysteresis gap was observed in the high-energy adsorption region ($p/p_0 < 0.005$). This behavior suggests that Mn^{2+} Lewis acid centers may enhance interactions with CO_2 at almost minimal surface coverage by accepting electron pairs, producing enough binding energy to introduce partial adsorption irreversibility [38].

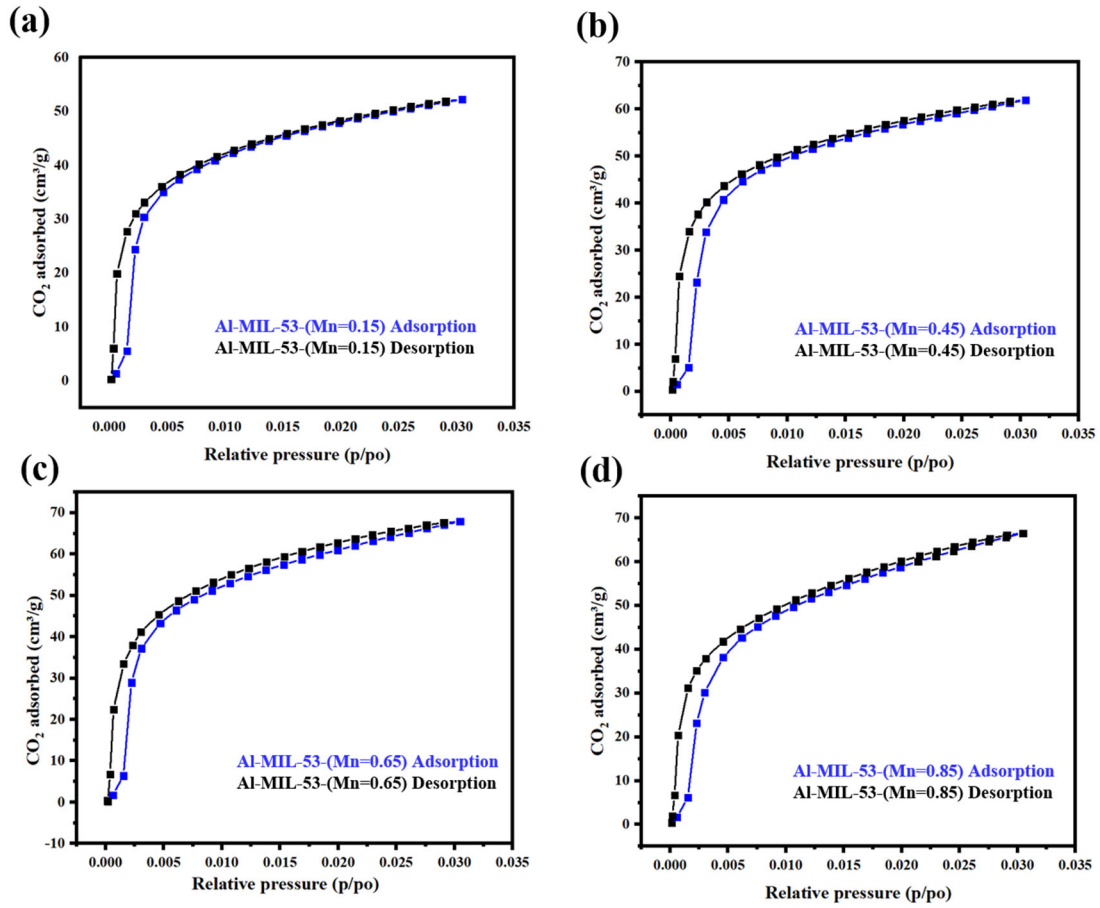


Figure 8. CO_2 adsorption and desorption isotherms on (**a**) Al-MIL-53-(Mn = 0.15), (**b**) Al-MIL-53-(Mn = 0.45), (**c**) Al-MIL-53-(Mn = 0.65), (**d**) Al-MIL-53-(Mn = 0.85).

CO_2 adsorption increased sharply up to 1 bar ($p/p_0 \approx 0.03$) as the Mn^{2+} content rose from 0.15 to 0.65, with Al-MIL-53-(Mn = 0.65) achieving a maximum uptake of 3.03 mmol/g, as shown in Table 3. Further increasing the Mn^{2+} ratio to 0.85 resulted in a comparable uptake of 2.97 mmol/g. The difference between these two samples (0.06 mmol/g, about 2%) is small, and these values alone cannot establish either as the better composition. The preference for Mn = 0.65 was based on the accompanying textural data: this sample shows the highest micropore content (67.9% vs. 53.4% for Mn = 0.85, Table 2) and the highest CO_2-DFT surface area (669.8 vs. 646.0 m^2/g, Table 3). The slightly lower uptake at Mn = 0.85, despite the considerably higher surface area reported in Table 2, is consistent with the emergence of minor mesoporosity at elevated Mn^{2+} loading. The dominant structural change is the loss of accessible microporosity, which directly limits CO_2 adsorption capacity. Such behavior aligns with previous findings that emphasize micropore volume as the critical determinant of adsorption performance in MIL-53 systems [47,48].

Table 3. Textural properties derived from low-pressure CO_2 adsorption on Al-MIL-53-(Mn).

Parameter	SA_{DFT} (m^2/g)	Pore Volume (cm^3/g)	Peak CO_2 Adsorbed (mmol/g)
Al-MIL-53-(Mn = 0.15)	522.9	0.116	2.33
Al-MIL-53-(Mn = 0.45)	612.9	0.144	2.76
Al-MIL-53-(Mn = 0.65)	669.8	0.155	3.03
Al-MIL-53-(Mn = 0.85)	646.0	0.160	2.97

3. Discussion

A Comparison of Al-MIL-53-(Mn = 0.65) Physicochemical Properties with Reported Pristine MIL-53(Al) and MOF Analogs

The primary effect of Mn incorporation was assessed primarily from the Mn/Al series, which was prepared, activated and measured under identical conditions in this study. A benchmark comparison of the physicochemical properties of Al-MIL-53-(Mn = 0.65) with those of reported pristine MIL-53(Al) and MOF analogs was performed. The assessment demonstrated that the primary contribution of the bimetallic system is in its intrinsic surface chemistry with the incorporation of the additional defect-induced binding sites involving Al^{3+} and Mn^{2+} Lewis centers, as well as enhanced stability (550 °C), as summarized in Table 4 [27,34,48,49]. Normalizing the recorded isotherm uptake against the available surface area sharpens the argument that the adsorbent is expected to outperform analogs at low pressures. The Al-MIL-53-(Mn = 0.65) framework delivers 3.03 mmol/g from only 347.8 m^2/g, corresponding to approximately 8.7 μmol of CO_2 per square meter of accessible surface, against roughly 1.3 and 1.9 $\mu mol/m^2$ for the two pristine MIL-53(Al) references (1631.9 m^2/g at 2.19 mmol/g and 1519 m^2/g at 2.85 mmol/g, respectively) and 0.9 $\mu mol/m^2$ for MIL-100(Cr) (1716 m^2/g, 1.6 mmol/g, although measured at 308 K and 1 atm). This indicates that the bimetallic framework matches or exceeds the reported pristine MIL-53(Al) uptakes while presenting less than a quarter of their surface area, giving a four- to six-fold higher areal adsorption efficiency [27,34]. The comparison therefore reframed the contribution of surface area in MOF performance as an upper bound on physisorptive capacity, whereas the chemical nature of open metal sites is expected to govern adsorption at the low CO_2 partial pressures relevant to flue gas [50].

This is further emphasized with the contrast to MIL-96(Al), whose surface area recorded at 353 m^2/g was also essentially similar to that of the current study's material, reaching 2.75 mmol/g, below the recorded 3.03 mmol/g of Al-MIL-53-(Mn = 0.65). This suggests that the increment in capacity of bimetallic MOFs is likely associated with the presence of additional coordinatively unsaturated sites and cannot be attributed to surface area alone. Similarly, it is clear that in Mn-BTT [51], in which Mn^{2+} was the sole Lewis acidic center, the single-metal MOF showed structural collapse at 350 °C, showing that Mn^{2+} in isolation is not sufficient to provide thermal stability [52]. The mixed-metal arrangement of Al^{3+}/Mn^{2+} therefore appeared to combine the complementary benefits of both metals: the Al^{3+}–μ_2-OH backbone preserves the orthorhombic MIL-53 topology and mechanical integrity, while the substituted Mn^{2+} centers introduce softer, more polarizable binding sites with a higher affinity for the quadrupole moment of CO_2 [53,54]. The different temperature profiles of the reported MOFs reinforced the same argument. The framework collapse temperature of 550 °C recorded for Al-MIL-53-(Mn = 0.65) is the highest among the materials compiled in Table 4**,** exceeding pristine MIL-53(Al) (450–500 °C), MIL-100(Cr) (450 °C), MIL-96(Al) (~400 °C) and Mn-BTT (350 °C). This range is practically significant for temperature swing desorption and provides substantial headroom for repeated thermal cycling without linker decarboxylation [55]. Combined with the retained rhomboidal crystal morphology and the preserved MIL-53 phase, these findings demonstrated that at an optimal metal ratio the development of bimetallic MOFs is a performance gain without the expense of structural integrity.

The scope was designed as a synthesis and screening investigation, aimed at establishing whether Mn^{2+} can be co-incorporated into the MIL-53(Al) framework without loss of phase integrity, and how the Mn^{2+}/Al^{3+} ratio affects the crystallinity, textural properties, thermal stability and equilibrium CO_2 uptake. Accordingly, CO_2 adsorption was assessed at a single screening temperature (273 K), and N_2 isotherms were recorded at 77 K for textural analysis only. Because single-component CO_2 and N_2 isotherms at 273 K and 298

K were not part of this screening dataset, the CO_2/N_2 selectivity and the isosteric heat of adsorption could not be derived, and the reported uptakes should be interpreted as indicators of relative performance within the series and against analogs from the literature, rather than as a direct measure of performance under flue-gas conditions. Similarly, EDX confirmed the co-existence of Al and Mn in all samples and, together with the M–O signals in FTIR and the peak shifts in PXRD, provides consistent evidence of Mn incorporation; however, EDX is a surface-sensitive, spot-based technique and cannot provide the bulk Mn content. The composition–property trends discussed in this work therefore refer to the nominal Mn^{2+}/Al^{3+} synthesis ratios, and bulk quantification of the retained Mn by ICP-OES is required to establish the actual framework composition.

Table 4. Overall comparative analysis of the physicochemical properties of reported pristine Al-MIL-53, other MOF analogs and Al-MIL-53-(Mn = 0.65).

Parameter	MIL-53(Al)	MIL-53(Al)	Mn-BTT	MIL-100(Cr)	MIL-96(Al)	Al-MIL-53-(Mn = 0.65)
Surface chemistry	Al^{3+} centers coordinated with terephthalate linkers and bridging –OH	Al^{3+} Lewis acid and bridging –OH along with carboxylates	Mn^{2+} Lewis centers	Cr^{3+} Lewis acid sites and terminal H_2O ligands	Dominated by Al^{3+} centers, hydroxyl groups, and carboxylate linkers	Al^{3+} and Mn^{2+} Lewis centers, bridging –OH, and carboxylates
Crystalline profile	Highly crystalline and well-defined orthorhombic MIL-53 structures	Highly crystalline with a pure MIL-53 phase	Stable and well-ordered crystalline structure, orthorhombic system	High crystallinity	High crystalline material with high order	Highly crystalline and pure MIL-53 phase (COD)
Morphology	Elongated rod-like crystals	Uniform rhomboidal shape	Not specified	Polyhedral crystals	Bifrustrum crystals	Rhomboidal crystals
Thermal stability profile	Major decomposition after 450 °C	Structural collapse from 500 °C	Degradation from 350 °C	Decomposition from 450 °C	Framework collapse from ~400 °C	Framework collapse from 550 °C
Textural properties	1631.9 m^2/g; 0.62 cc/g; microporous	1519 m^2/g, 0.778 cc/g, microporous	Not specified	1716 m^2/g, 0.79 cc/g, predominantly microporous	353 m^2/g, microporous	347.8 m^2/g, 0.174 cc/g, predominantly microporous
CO_2 uptake at 273K and 1 bar	2.19 mmol/g	2.85 mmol/g	Not specified	1.6 mmol/g (at 308 K, 1 atm)	2.75 mmol/g	3.03 mmol/g
References	[34]	[27]	[51]	[56]	[57]	Current study

4. Materials and Methods

4.1. Materials

Analytical grade chemicals, including aluminum nitrate nonahydrate ($Al(NO_3)_3{\cdot}9H_2O$, 98%), manganese nitrate tetrahydrate ($Mn(NO_3)_2{\cdot}4H_2O$, 97%), and benzene-1,4-dicarboxylic acid ($C_8H_6O_4$, TPA, 98%), were used for the synthesis of the bimetallic MOF, with the two metal nitrates used as metal precursors and the acid as the functional organic linker. Dimethylformamide (C_3H_7NO, 98.9%) and anhydrous ethanol (C_2H_6O, 98%) were utilized for washing purposes, and deionized water (DI water, H_2O) was the mother liquor. All reagents were purchased from Protea Laboratory Solutions (Pty) Ltd., Johannesburg, South Africa, including products from Sisco Research Laboratories Pvt. Ltd., Maharashtra, India and Sigma-Aldrich, Madrid, Spain. DI water was sourced in-house through the chemical engineering laboratory reverse osmosis system.

4.2. Hydrothermal Synthesis

The bimetallic Al-MIL-53-(Mn) samples were synthesized according to previously reported methods in the literature using a hydrothermal regime [12,23,29,34]. Typically, a series of samples were synthesized at Mn^{2+}/Al^{3+} molar ratios varied as 0.15, 0.45, 0.65, and 0.85, yielding Al-MIL-53-(Mn = 0.15), Al-MIL-53-(Mn = 0.45), Al-MIL-53-(Mn = 0.65), and Al-MIL-53-(Mn = 0.85), respectively, which were classified as low, moderate, and high loading. These ratios are nominal values based on the composition of the synthesis mixture and serve only as sample labels; they do not represent the final metal composition of the activated materials. Aluminum nitrate nonahydrate ($Al(NO_3)_3{\cdot}9H_2O$), manganese nitrate tetrahydrate ($Mn(NO_3)_2{\cdot}4H_2O$), terephthalic acid (TPA), and DI water were stirred for 15 min at room temperature until complete dispersion was achieved. After this first homogenization step, the mixture was exposed to 40 kHz ultrasonic waves for 40 min to enhance the homogeneity of the solution. Subsequently, the well-dispersed reactant mixture was transferred to 250 mL autoclaves with Teflon liners and steel and placed in a forced-air oven to heat the sample to 180 °C for 72 h to achieve high crystallization. The standard synthesis temperature of monometallic MIL-53 of 220 °C was reduced to 180 °C to account for the presence of Mn^{2+}, which requires milder synthesis temperatures to prevent oxidation [37,58]. Following the aforementioned steps, the autoclaves were allowed to cool naturally at room temperature, and thereafter, the solid phase was separated from the mother liquor by a centrifuge and washed with DI water to remove surface-trapped reactants. All experiments were conducted with a constant metal-to-ligand ratio of 2:1 and a solid reactant to solvent ratio of 1:3.27 by mass.

4.3. Two-Step Activation

Following the solid-phase separation, 40 mL of DMF (liquid solvent) was added to the solid paste. The mixture was stirred for 10 min at 400 rpm and transferred back to the autoclaves to be heated to 150 °C for 24 h [29]. Thereafter, the obtained product was separated by centrifugation and washed with 20 mL of ethanol three times, followed by continuous immersion in 35 mL of ethanol for 48 h, with the ethanol replenished every 12 h to ensure thorough removal of residual solvent. Lastly, the solid phase was subjected to vacuum heating at 150 °C for 12 h [14]. The hydrothermal synthesis and two-step activation procedures are summarized in Figure 9.

4.4. Characterization Techniques

Conventional characterization techniques including FTIR (PerkinElmer FTIR Frontier Spectrum 100; PerkinElmer, Waltham, MA, USA) at a frequency range of 400–4000 cm^{-1}, PXRD (Rigaku Ltd. Diffractometer; Rigaku Corporation, Tokyo, Japan) with $\lambda CuK\alpha$ = 1.54056 Å and a step size of 0.05° at 40 kV and 30 mA (d-spacings and crystalline domain sizes (D) of the (110) reflection were calculated from Bragg's law, $n\lambda = 2d \sin\theta$, and the Scherrer equation, $D = K\lambda/(\beta \cos\theta)$, with K = 0.9 and β the FWHM in radians), SEM-EDX (HRSEM JSM 7900 FS; JEOL Ltd., Tokyo, Japan) at a magnifications of x5000 and x2000, TGA (SDT Q600 V20.9 Build 20; TA Instruments, New Castle, DE, USA) using a dual ramp method overin a temperature range of 0 to 1000 °C and low-pressure N_2 and CO_2 adsorption (Anton Paar NOVA 800 BET; Anton Paar GmbH, Graz, Austria) under vacuum, followed by analysis and then analyzed using pure N_2 (77 K) and CO_2 (273 K) to obtain the isotherms and textural properties.

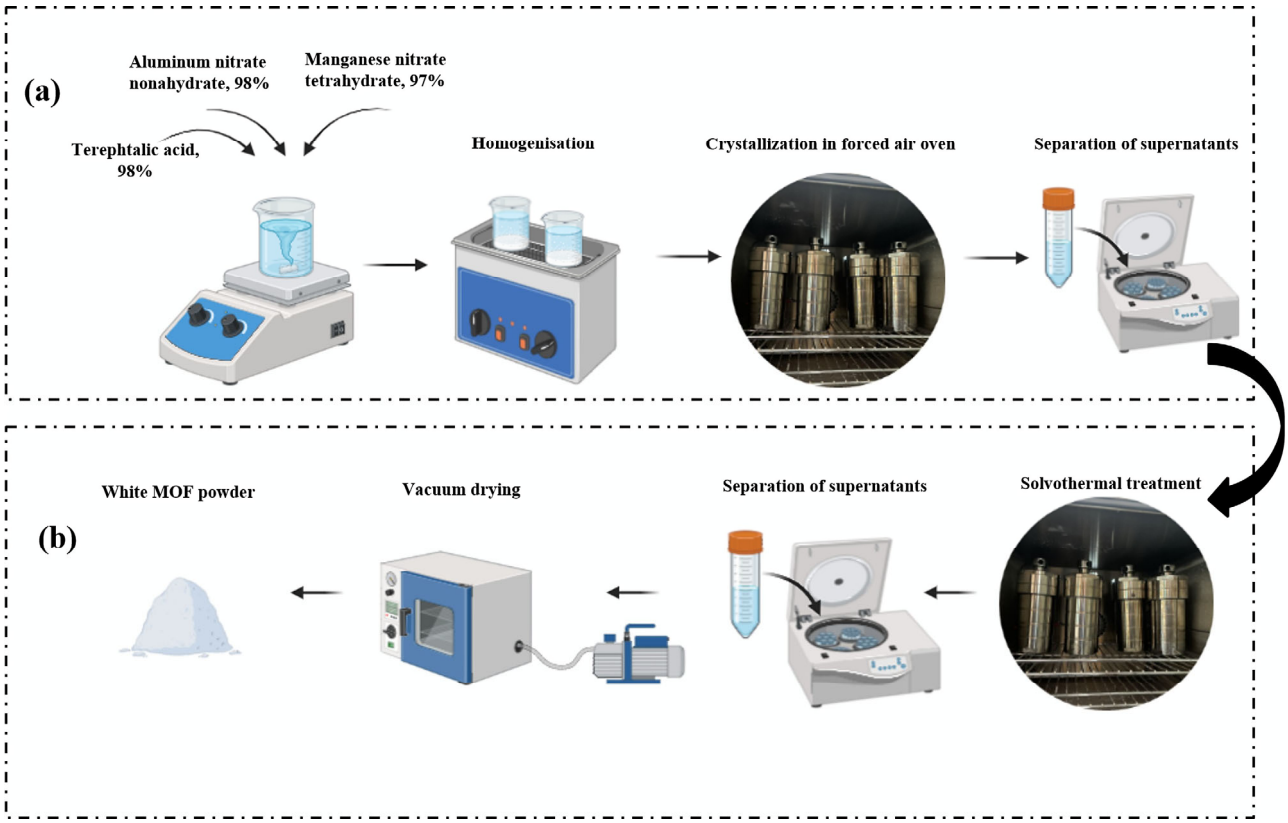


Figure 9. Summarized schematic diagram depicting (**a**) the hydrothermal synthesis and (**b**) the two-step activation.

5. Conclusions

The physicochemical characterization confirmed the successful development of a mixed-metal MOF, reflecting the characteristics of typical MIL-53 structures with predominant $AlO_4(OH)_2$ chains. Such MOF materials are associated with high performance; the superior sample in this study demonstrated 3.03 mmol/g at 273 K and 1 bar. Moreover, a comparative assessment of the obtained physicochemical properties with the existing literature revealed that the fundamental contribution of this approach lies in the surface chemistry and thermal stability, where the BMOF possesses heterogeneous metal centers and withstands up to 550 °C. The mixed-metal synthesis ratio suggested an initial positive effect, demonstrated by the gradual increase in crystallinity, followed by framework destabilization at high Mn^{2+} loading. Moreover, the N_2 and CO_2 adsorption measurements showed increased micropore content spanning from 58.2% for Al-MIL-53-(Mn = 0.15) to 67.9% for the Al-MIL-53-(Mn = 0.65) before a decrease to 53.4% for the Al-MIL-53-(Mn = 0.85), collectively suggesting that a moderate Mn^{2+}/Al^{3+} ratio of 0.65 was the most favorable composition within this series, although its CO_2 uptake (3.03 mmol/g) was comparable to that at 0.85 (2.97 mmol/g). This is a critical finding for future mixed-metal development. Future work should consider the extension of the adsorption assessment of this framework beyond single-temperature and single-component equilibrium isotherms towards application-oriented conditions, including single-component CO_2 and N_2 isotherms at 273 K and 298 K and at real flue-gas temperatures (313–333 K), multicomponent CO_2/N_2 and CO_2/CH_4 binary selectivity measurements, heats of adsorption and dynamic experiments in packed columns under humid conditions. Further, the considerably high collapse temperature of the bimetallic framework invites investigations of whether the mixed-metal nodes improve the moisture stability of the obtained adsorbent, as this remains one of the fundamental drawbacks to the wide implementation of MOFs in industrial applications. Additionally, further development should consider bulk quantification of the retained Mn

by ICP-OES analysis and advanced characterization techniques, such as XPS and X-ray absorption spectroscopy, to establish the local coordination environment of Mn within the framework.

Author Contributions: Conceptualization, B.D., M.M.M. and T.P.; methodology, B.D., M.M.M. and T.P.; formal analysis, B.D.; investigation, B.D.; resources, M.M.M. and T.P.; data curation, B.D.; writing—original draft preparation, B.D., O.R.O., M.M.M. and T.P.; writing—review and editing, M.M.M. and T.P.; supervision; funding acquisition, M.M.M. All authors have read and agreed to the published version of the manuscript.

Funding: This work was supported by the National Research Foundation of South Africa (NRF—Grant No.: TTK250322305772).

Data Availability Statement: Raw data supporting the presented findings are available upon request to the corresponding author.

Acknowledgments: We gratefully acknowledge the University of Johannesburg's Faculty of Engineering and the Built Environment and the Department of Chemical Engineering.

Conflicts of Interest: The authors declare no conflicts of interest.

Abbreviations

The following abbreviations are used in this manuscript:

CCDC	Cambridge Crystallographic Data Centre
COD	Crystallography Open Database
FTIR	Fourier Transform Infrared Spectroscopy
IUPAC	International Union of Pure and Applied Chemistry
OMS	Open metal sites
PSM	Post-synthetic modification
PXRD	Powder X-ray Diffraction
SBUs	Secondary building unit(s)
SEM-EDX	Scanning Electron Microscopy–Energy Dispersive X-Ray spectroscopy
TGA	Thermogravimetric Analysis

References

1. Zentou, H.; Aliyu, M.; Abdalla, M.A.; Abdelaziz, O.Y.; Hoque, B.; Alloush, A.M.; Tayeb, I.M.; Patchigolla, K.; Abdelnaby, M.M. Advancements and challenges in adsorption-based carbon capture technology: From fundamentals to deployment. *Chem. Rec.* **2025**, *25*, e202400188.
2. Raganati, F.; Miccio, F.; Ammendola, P. Adsorption of carbon dioxide for post-combustion capture: A review. *Energy Fuels* **2021**, *35*, 12845–12868.
3. Dhoke, C.; Zaabout, A.; Cloete, S.; Amini, S. Review on reactor configurations for adsorption-based CO_2 capture. *Ind. Eng. Chem. Res.* **2021**, *60*, 3779–3798.
4. Kumari, S.; Gusain, M.; Lamba, B.Y.; Kumar, S. A critical review on recent advancements in metal–organic frameworks for CO_2 capture, storage and utilization. *J. Mater. Chem. A* **2025**, *13*, 21352–21388.
5. Kim, J.H.; Yun, H.; Kim, C.G.; Kim, N.; Yang, Y.; Yoo, S.; Moon, D.; Kim, D.; Hong, C.S. Postsynthetic Triazolate Functionalization of Ni2Cl2BTDD: Creation of Supplementary CO_2 Adsorption Sites and Exceptional CO_2 Selectivity. *J. Am. Chem. Soc.* **2025**, *147*, 37732–37740.
6. Jun, H.J.; Yoo, D.K.; Jhung, S.H. Metal-organic framework (MOF-808) functionalized with ethyleneamines: Selective adsorbent to capture CO_2 under low pressure. *J. CO2 Util.* **2022**, *58*, 101932.
7. Wei, R.; Zhao, T.; Xu, H.; Gao, J. Recent advances and challenges of metal–organic frameworks for CO_2 capture. *Dalton Trans.* **2025**, *54*, 8385–8391.

8. Geary, J.; Xiao, D.J. Engineering bimetallic active sites in metal–organic frameworks: Challenges and opportunities. *Chem. Mater.* **2024**, *36*, 4916–4928.
9. Liu, S.; Qiu, Y.; Liu, Y.; Zhang, W.; Dai, Z.; Srivastava, D.; Kumar, A.; Pan, Y.; Liu, J. Recent advances in bimetallic metal–organic frameworks (BMOFs): Synthesis, applications and challenges. *New J. Chem.* **2022**, *46*, 13818–13837.
10. Chen, C.; Kosari, M.; Jing, M.; He, C. Microwave-assisted synthesis of bimetallic NiCo-MOF-74 with enhanced open metal site for efficient CO_2 capture. *Environ. Funct. Mater.* **2022**, *1*, 253–266.
11. Chen, L.; Wang, H.-F.; Li, C.; Xu, Q. Bimetallic metal–organic frameworks and their derivatives. *Chem. Sci.* **2020**, *11*, 5369–5403.
12. Abid, H.R.; Rada, Z.H.; Liu, L.; Wang, S.; Liu, S. Striking CO_2 capture and CO_2/N_2 separation by Mn/Al bimetallic MIL-53. *Polyhedron* **2021**, *193*, 114898.
13. Loiseau, T.; Volkringer, C.; Haouas, M.; Taulelle, F.; Ferey, G. Crystal chemistry of aluminium carboxylates: From molecular species towards porous infinite three-dimensional networks. *Comptes Rendus. Chimie* **2015**, *18*, 1350–1369.
14. Sun, L.; Yin, M.; Li, Z.; Tang, S. Facile microwave-assisted solvothermal synthesis of rod-like aluminum terephthalate [MIL-53(Al)] for CO_2 adsorption. *J. Ind. Eng. Chem.* **2022**, *112*, 279–286.
15. Han, B.; Chakraborty, A. Functionalization, protonation and ligand extension on MIL-53 (Al) MOFs to boost water adsorption and thermal energy storage for heat transformations. *Chem. Eng. J.* **2023**, *472*, 145137.
16. Sundriyal, S.; Shrivastav, V.; Sharma, M.; Mishra, S.; Deep, A. Redox additive electrolyte study of Mn–MOF electrode for supercapacitor applications. *ChemistrySelect* **2019**, *4*, 2585–2592.
17. Deng, S.; Xu, B.; Zhao, J.; Kan, C.W.; Liu, X. Unlocking Double Redox Reaction of Metal–Organic Framework for Aqueous Zinc-Ion Battery. *Angew. Chem. Int. Ed.* **2024**, *63*, e202401996.
18. Asghar, A.; Iqbal, N.; Noor, T.; Kariuki, B.M.; Kidwell, L.; Easun, T.L. Efficient electrochemical synthesis of a manganese-based metal–organic framework for H_2 and CO_2 uptake. *Green Chem.* **2021**, *23*, 1220–1227.
19. Chen, Z.; Xiao, Y.; Liu, X.; Lu, H.; Wang, X.; Ding, G.; Wang, Z.; Wang, P.; Liao, G.; Chen, L. Emerging Bimetallic Metal-Organic Frameworks for Photocatalytic Carbon Dioxide Reduction. *Coord. Chem. Rev.* **2026**, *556*, 217704.
20. Dolgopolova, E.A.; Brandt, A.J.; Ejegbavwo, O.A.; Duke, A.S.; Maddumapatabandi, T.D.; Galhenage, R.P.; Larson, B.W.; Reid, O.G.; Ammal, S.C.; Heyden, A. Electronic properties of bimetallic metal–organic frameworks (MOFs): Tailoring the density of electronic states through MOF modularity. *J. Am. Chem. Soc.* **2017**, *139*, 5201–5209.
21. Luo, L.; Qian, X.; Wang, X. Bimetallic metal-organic frameworks and their derivatives for electrochemical energy conversion and storage: Recent progress, challenges and perspective. *J. Energy Storage* **2024**, *98*, 113052.
22. López-García, C.; Canossa, S.; Hadermann, J.; Gorni, G.; Oropeza, F.E.; De La Peña O'Shea, V.A.; Iglesias, M.; Monge, M.A.; Gutiérrez-Puebla, E.; Gándara, F. Heterometallic Molecular Complexes Act as Messenger Building Units to Encode Desired Metal-Atom Combinations to Multivariate Metal–Organic Frameworks. *J. Am. Chem. Soc.* **2022**, *144*, 16262–16266.
23. Wang, H.; Jiang, Y.; Han, R.; Liu, Q.; Liu, C. Facile preparation of Al/Mn bimetallic metal-organic frameworks for removing trace benzene indoor. *Sep. Purif. Technol.* **2025**, *354*, 128625.
24. Millucci, F.; Germani, R.; Colelli, L.; Gabrielli, S.; Sassi, P.; Donnadio, A.; Conti, M.; Corezzi, S. Overcoming hydrophobicity with water enables ultrafast hydrolysis of waste polyethylene terephthalate at very mild conditions. *Angew. Chem.* **2026**, *138*, e14136.
25. Kökçam-Demir, Ü.; Goldman, A.; Esrafili, L.; Gharib, M.; Morsali, A.; Weingart, O.; Janiak, C. Coordinatively unsaturated metal sites (open metal sites) in metal–organic frameworks: Design and applications. *Chem. Soc. Rev.* **2020**, *49*, 2751–2798.
26. Chuang, C.H.; Seong, J.; Hsiao, L.W.; Lin, C.Y.; Liu, C.L.; Lee, J.S.; Kang, D.Y. Critical Role in Structural Optimization and Activation of CAU-23 Membranes for CO_2 Separation. *Small* **2025**, *21*, e09215.
27. Abid, H.R.; Rada, Z.H.; Shang, J.; Wang, S. Synthesis, characterization, and CO_2 adsorption of three metal-organic frameworks (MOFs): MIL-53, MIL-96, and amino-MIL-53. *Polyhedron* **2016**, *120*, 103–111.
28. Fan, D.; Oliveira, F.L.; Bonakala, S.; Wahiduzzaman, M.; Maurin, G. Decoding local framework dynamics in the ultra-small pore MOF MIL-120 (Al) CO_2 adsorbent using machine-learning potential. *Nat. Commun.* **2026**, *17*, 3235.
29. Ahadi, N.; Askari, S.; Fouladitajar, A.; Akbari, I. Facile synthesis of hierarchically structured MIL-53 (Al) with superior properties using an environmentally-friendly ultrasonic method for separating lead ions from aqueous solutions. *Sci. Rep.* **2022**, *12*, 2649.
30. Rehman, T.U. Exploring the Photoluminescence and Structural insights of MIL-53 (Al) Metal-Organic Framework Under Multi-Stimulus Environment. Ph.D. Thesis, University of Palermo, Palermo, Italy, 2025.

31. Hadjiivanov, K.I.; Panayotov, D.A.; Mihaylov, M.Y.; Ivanova, E.Z.; Chakarova, K.K.; Andonova, S.M.; Drenchev, N.L. Power of infrared and Raman spectroscopies to characterize metal-organic frameworks and investigate their interaction with guest molecules. *Chem. Rev.* **2020**, *121*, 1286–1424.
32. Yan, J.; Jiang, S.; Ji, S.; Shi, D.; Cheng, H. Metal-organic framework MIL-53 (Al): Synthesis, catalytic performance for the Friedel-Crafts acylation, and reaction mechanism. *Sci. China Chem.* **2015**, *58*, 1544–1552.
33. Deng, L.; Liu, P.; Xiao, H.; Zhu, X.; Wang, Y.; Duan, L.; Duan, X.; Wen, Y.; Kong, Z.; Xu, J. In-situ architecting hydrophilic, defect-rich MgMn-MOF on bimetallic oxide loaded biochar for smartphone-operated portable electrochemical-colorimetric dual-mode intelligent sensing of Cu^{2+} in rice plants. *Sens. Actuators B Chem.* **2025**, *439*, 137859.
34. Abid, H.R.; Znad, H.; Alawi, N.M.; Rashid, F.L.; Dulaimi, A.; Alanazi, A.; Keshavarz, A.; Iglauer, S.; Wang, S. Enhancing CO_2 Adsorption and CO_2/N_2 Separation Performance by Incorporating Calcium in MIL-53 (Al). *Int. J. Environ. Res.* **2026**, *20*, 97.
35. Mihaylov, M.; Chakarova, K.; Andonova, S.; Drenchev, N.; Ivanova, E.; Sabetghadam, A.; Seoane, B.; Gascon, J.; Kapteijn, F.; Hadjiivanov, K. Adsorption forms of CO_2 on MIL-53 (Al) and NH_2-MIL-53 (Al) as revealed by FTIR spectroscopy. *J. Phys. Chem. C* **2016**, *120*, 23584–23595.
36. Bon, V.; Busov, N.; Senkovska, I.; Bönisch, N.; Abylgazina, L.; Khadiev, A.; Novikov, D.; Kaskel, S. The importance of crystal size for breathing kinetics in MIL-53 (Al). *Chem. Commun.* **2022**, *58*, 10492–10495.
37. Salionov, D.; Semivrazhskaya, O.O.; Casati, N.P.; Ranocchiari, M.; Bjelić, S.; Verel, R.; van Bokhoven, J.A.; Sushkevich, V.L. Unraveling the molecular mechanism of MIL-53 (Al) crystallization. *Nat. Commun.* **2022**, *13*, 3762.
38. Abid, H.R.; Rada, Z.H.; Li, Y.; Mohammed, H.A.; Wang, Y.; Wang, S.; Arandiyan, H.; Tan, X.; Liu, S. Boosting CO_2 adsorption and selectivity in metal–organic frameworks of MIL-96 (Al) via second metal Ca coordination. *RSC Adv.* **2020**, *10*, 8130–8139.
39. Athar, M.; Rzepka, P.; Thoeny, D.; Ranocchiari, M.; van Bokhoven, J.A. Thermal degradation of defective high-surface-area UiO-66 in different gaseous environments. *RSC Adv.* **2021**, *11*, 38849–38855.
40. Yu, Q.; Xia, Z.; Zhou, X.; Ma, N.; Dai, W. Hierarchically Porous Bimetallic Dual-Metal–Organic Frameworks for Synergistic and Selective Adsorption of Thiophenic Sulfur: A Density Functional Theory-Validated Metal–Sulfur Coordination Mechanism. *Langmuir* **2025**, *41*, 29589–29605.
41. Sofi, F.A.; Bhat, M.A.; Majid, K. Cu^{2+}-BTC based metal–organic framework: A redox accessible and redox stable MOF for selective and sensitive electrochemical sensing of acetaminophen and dopamine. *New J. Chem.* **2019**, *43*, 3119–3127.
42. Bonakala, S.; Abutaha, A.; Elumalai, P.; Samara, A.; Mansour, S.; El-Mellouhi, F. Democratizing the Assessment of Thermal Robustness of Metal–Organic Frameworks. *ACS Omega* **2022**, *7*, 46515–46523.
43. Healy, C.; Patil, K.M.; Wilson, B.H.; Hermanspahn, L.; Harvey-Reid, N.C.; Howard, B.I.; Kleinjan, C.; Kolien, J.; Payet, F.; Telfer, S.G. The thermal stability of metal-organic frameworks. *Coord. Chem. Rev.* **2020**, *419*, 213388.
44. García-Ben, J.; López-Beceiro, J.; Artiaga, R.; Salgado-Beceiro, J.; Delgado-Ferreiro, I.; Kolen'ko, Y.V.; Castro-García, S.; Señarís-Rodríguez, M.A.; Sánchez-Andújar, M.; Bermúdez-García, J.M. Discovery of colossal breathing-caloric effect under low applied pressure in the hybrid organic–inorganic MIL-53 (Al) material. *Chem. Mater.* **2022**, *34*, 3323–3332.
45. Cui, P.; Tang, Y.; Guo, A.; Wang, C.; Liu, M.; Peng, W.; Yu, F. Enhanced CO_2 adsorption properties with bimetallic ZnCe-MOF prepared using a microchannel reactor. *Front. Chem. Sci. Eng.* **2025**, *19*, 14.
46. Makuwa, G.N.; Mabuza, M.M. A Modified Approach for the Synthesis of Magnesium-and Zinc-Based Metal–Organic Frameworks for Carbon Capture: Probing the Physicochemical Properties. *Processes* **2026**, *14*, 967.
47. Khan, A.U.; Othman, M.H.D.; Younas, M.; Puteh, M.H.; Rahman, M.A.; Jaafar, J. Synthesis and characterization of bimetallic mof hkust-1 (cu, Mg) adsorbents and their application in natural gas purification. *ASEAN Eng. J.* **2024**, *14*, 153–160.
48. Pendleton, P.; Badalyan, A.; Bromball, R.; Skinner, W. Effect of oxidizing agent on activated carbon cloth porosity and surface chemistry. In *Studies in Surface Science and Catalysis*; Elsevier: Amsterdam, The Netherlands, 2007; pp. 575–582.
49. Zhang, Y.; Lucier, B.E.; Huang, Y. Deducing CO_2 motion, adsorption locations and binding strengths in a flexible metal–organic framework without open metal sites. *Phys. Chem. Chem. Phys.* **2016**, *18*, 8327–8341.
50. Kazemi, A.; Pordsari, M.A.; Tamtaji, M.; Afshari, M.H.; Keshavarz, S.; Zeinali, F.; Baesmat, H.; Zahiri, S.; Manteghi, F.; Ghaemi, A. Unveiling the power of defect engineering in MOF-808 to enhance efficient carbon dioxide adsorption and separation by harnessing the potential of DFT analysis. *Chem. Eng. J.* **2024**, *494*, 153049.
51. Dincă, M.; Dailly, A.; Liu, Y.; Brown, C.M.; Neumann, D.A.; Long, J.R. Hydrogen Storage in a Microporous Metal–Organic Framework with Exposed Mn^{2+} Coordination Sites. *J. Am. Chem. Soc.* **2006**, *128*, 16876–16883.
52. Bi, F.; Feng, X.; Zhou, Z.; Zhang, Y.; Wei, J.; Yuan, L.; Liu, B.; Huang, Y.; Zhang, X. Mn-based catalysts derived from the non-thermal treatment of Mn-MIL-100 to enhance its water-resistance for toluene oxidation: Mechanism study. *Chem. Eng. J.* **2024**, *485*, 149776.

53. Yang, D.; Gates, B.C. Characterization, Structure, and Reactivity of Hydroxyl Groups on Metal-Oxide Cluster Nodes of Metal–Organic Frameworks: Structural Diversity and Keys to Reactivity and Catalysis. *Adv. Mater.* **2024**, *36*, 2305611.
54. Esfandian, H.; Ebneyamini, M.; Darzi, F.Z. Ligand ratio engineering in manganese-based metal–organic frameworks for high-performance supercapacitors. *Sci. Rep.* **2026**, *16*, 37250.
55. Gholami, M.; Van Assche, T.R.; Denayer, J.F. Temperature vacuum swing, a combined adsorption cycle for carbon capture. *Curr. Opin. Chem. Eng.* **2023**, *39*, 100891.
56. Cabello, C.P.; Berlier, G.; Magnacca, G.; Rumori, P.; Palomino, G.T. Enhanced CO_2 adsorption capacity of amine-functionalized MIL-100 (Cr) metal–organic frameworks. *CrystEngComm* **2014**, *17*, 430–437.
57. González-Santiago, B.; García-Carrillo, A.; Chávez-Guerrero, L.; Poisot, M.; Lemus-Santana, A.A.; García-Sánchez, M.Á.; Medina-Juárez, O. Enhancing the synthetic routes to prepare MIL-96(Al) and their efficiency for CO_2 capture. *Inorg. Chem. Commun.* **2023**, *155*, 111095.
58. Abazari, R.; Sanati, S.; Nanjundan, A.K.; Wang, Q.; Dubal, D.P.; Liu, M. Structure–property–performance relationship of vanadium-and manganese-based metal–organic frameworks and their derivatives for energy storage and conversion applications. *J. Mater. Chem. A* **2024**, *12*, 11149–11175.

Disclaimer/Publisher's Note: The statements, opinions and data contained in all publications are solely those of the individual author(s) and contributor(s) and not of MDPI and/or the editor(s). MDPI and/or the editor(s) disclaim responsibility for any injury to people or property resulting from any ideas, methods, instructions or products referred to in the content.